ENGINEERING

Snapping for high-speed and high-efficient butterfly stroke–like soft swimmer

Yinding Chi, Yaoye Hong, Yao Zhao, Yanbin Li, Jie Yin*

Natural selection has tuned many flying and swimming animals to share the same narrow design space for high power efficiency, e.g., their dimensionless Strouhal numbers St that relate flapping frequency and amplitude and forward speed fall within the range of 0.2 < St < 0.4 for peak propulsive efficiency. It is rather challenging to achieve both comparably fast-speed and high-efficient soft swimmers to marine animals due to the naturally selected narrow design space and soft body compliance. Here, bioinspired by the flapping motion in swimming animals, we report leveraging snapping instabilities for soft flapping-wing swimmers with comparable high performance to biological counterparts. The lightweight, butterfly stroke–like soft swimmer (2.8 g) demonstrates a record-high speed of 3.74 body length/s (4.8 times faster than the reported fastest flapping soft swimmer), high power efficiency (0.2 < St = 0.25 < 0.4), low energy consumption cost, and high maneuverability (a high turning speed of 157°/s).

INTRODUCTION

Flapping motion is a fast yet energy-efficient locomotion mode in flyers and swimmers such as birds, insects, and marine animals (*1*, *2*). They leverage bending and/or rotating flexible wings, fins, body, or tails for passively increasing propulsion efficiency to save energy (*2*). Among them, many are observed to cruise in a narrow range of dimensionless Strouhal number St, defined as St = fA/U (*f* and *A* are flapping frequency and amplitude and *U* is forward velocity), i.e., 0.2 < St < 0.4 for high power efficiency (*3*, *4*). Bioinspired by these flyers and swimmers, various aqueous soft robots have been created. They use similar flapping or oscillation motions for propulsion driven by various fluidic, electrical, and photoactive soft actuators (*5*–*8*). However, their performances are far from competing with marine animals in terms of both speed *U* [*U* < 1 body length per second (BL/s) in soft robots (*5*) versus 2 to 24 BL/s in marine animals (*9*)] and propulsion efficiency (St > 1 or St < 0.1 in soft robots versus 0.2 < St < 0.4 in marine animals) (*6*–*8*, *10*, *11*). It remains a grand challenge to achieve both fast and high-efficient aqueous soft robots with high performance comparable to their biological counterparts due to the compliance of their soft body (*12*) and the naturally selected narrow design space (St) for high propulsive efficiency.

To address the challenge, we exploit leveraging snapping of bistable flexible wings for amplified aqueous performances in a soft-bodied flapping-wing swimmer. Snapping is a fast motion that is often observed in nature [e.g., fast closure of Venus flytraps (*13*)] and in daily life (e.g., popper jumping toys and hair clippers). These structures have two stable shapes, i.e., bistable structures. They can snap reversibly from one stable shape to the other reverted stable shape within tens of milliseconds and remain in either stable state without energy consumption.

Recently, harnessing bistability for high-performance soft robots has attracted growing interest in addressing the soft body compliance–related issues such as slow response and small force (*5*, *14*–*20*). Bistability enables fast response and amplified force in soft actuators via quick energy release during snapping (*21*). This is especially attractive for aquatic biomimetic soft robotics, where a relatively larger force is often required to overcome much higher water resistance than on ground and in air (*21*). Bioinspired by the aquatic animals, a recent study has demonstrated harnessing bistable elements for untethered, directional propulsion of soft robots (*19*). The fast linear motion in the bistable von Mises truss element is actuated by shape memory polymer muscles to drive the paddling of attached fins for propulsion. However, the swimming remains challenging to be sustainable without varying the water temperature (*19*). Very recently, by leveraging bistable compliant mechanisms for flapping a soft robotic fish's body, we have achieved a fast swimming speed of 0.78 BL/s at a low pneumatic actuation frequency of 1.3 Hz (*5*). Despite these advances, soft swimmers with comparable high performances to their biological counterparts have yet to be realized (*5*–*8*, *10*, *11*, *22*–*26*).

Here, we present a generic design of bistable and multistable soft flapping actuators composed of soft bending actuators and precurved flexible wings (Fig. 1). Inspired by the design of hair clippers, the soft flapping actuator is constructed by bonding two parallel wing frame ribbons at the tip to form a pair of bistable precurved flexible wings (Fig. 1A). The actuated small flexion of the soft body can drive the passive snapping of the wings for largely amplified flapping and rotating motions. We explore the generic design principle and dynamic flapping performances of the bistable soft actuators through combined experimental characterization, finite element simulation, and theoretical modeling. Leveraging the knowledge, we exploit harnessing bistability and multistability for high-speed, high energy-efficient, and maneuverable soft swimmers.

RESULTS

Design and working principles of bistable and multistable soft flapping actuators

Figure 1A and fig. S1 show the schematic design and fabrication of a bistable soft flapping actuator. It is composed of a soft body and two attached bistable flexible ribbon frame–based wings (see Materials and Methods for details). The soft body (*L* = 22.8 mm by *W* = 10 mm by *T* = 6.55 mm) is an elastomeric pneumatic bidirectional

Department of Mechanical and Aerospace Engineering, North Carolina State University, Raleigh, NC 27695, USA.
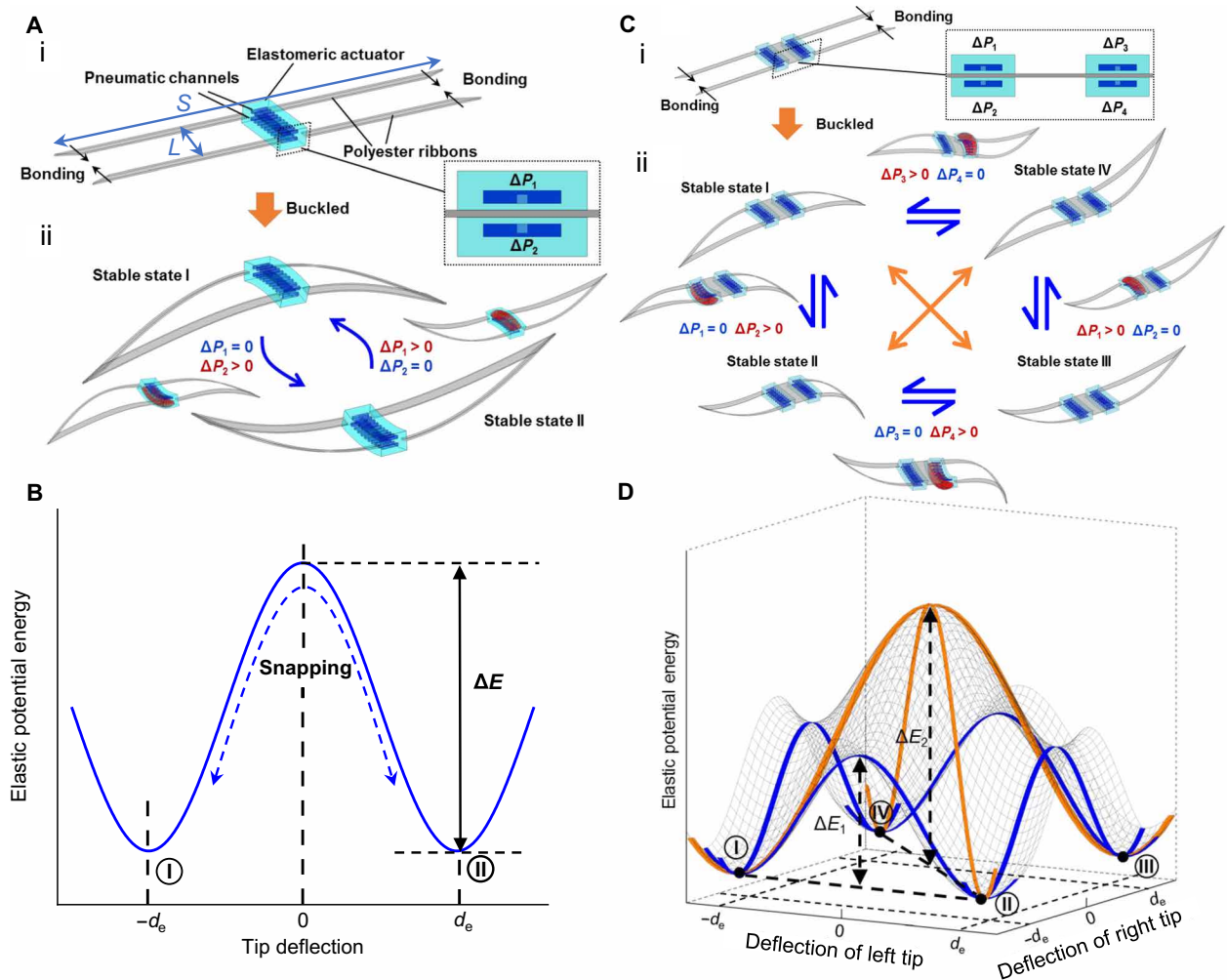*Corresponding author. Email: jyin8@ncsu.edu

Fig. 1. Design and working principles of bistable and multistable soft flapping actuators. (**A**) Schematic design of a precurved bistable soft flapping actuator by bonding the tips of two parallel polyester ribbons (as a bistable wing frame) sandwiched by a bidirectional pneumatic soft bending actuator in the middle (as soft body) (i). Pneumatic actuation of either top ($\Delta P_1 > 0$) or bottom air channels ($\Delta P_2 > 0$) leads to the fast bistable state switch to flap the wings (ii). (**B**) Schematic of energy landscape of the bistable flapping actuator. (**C**) Schematic design of a multistable soft flapping actuator by bonding the tips of wings sandwiched by two parallel pneumatic soft bending actuators in the middle (i). It allows independent actuation of flapping either bistable wing to reversibly switch between four stable states under single (blue arrows) or double (orange arrows) actuation mode as illustrated in (ii). (**D**) Schematics of energy landscape of the multistable flapping actuator with four localized minimum energy states. The snap-through deformation can only follow the colored paths in the landscape. The blue curves correspond to single actuation mode with energy barrier ΔE_1, and the orange curves correspond to dual actuation mode with energy barrier $\Delta E_2 = 2 \Delta E_1$.

bending actuator made of Ecoflex, which has two embedded spine-shaped pneumatic channels on top and bottom (fig. S2). The soft body can flex upward and downward upon pressurizing the bottom ($\Delta P_2 > 0$) and top chamber ($\Delta P_1 > 0$), respectively (Fig. 1Aii). The flexible frame of two wings takes an initial planar "H"-like shape by bridging two parallel, long polyester ribbons with an elastomeric plate in the middle. Then, it is sandwiched in between the soft pneumatic bending actuator (Fig. 1Ai, and fig. S1) to form a one-piece structure. The length of the ribbon defines the wingspan length S. Then, bonding two tips of the H-shaped ribbons introduces both lateral torsion and compression deformation, resulting in out-of-plane buckling of the two jointed ribbons into a bended and twisted wing frame. Consequently, it forms a soft flapping actuator with a pair of bistable precurved framed wings with prestored elastic strain energy (Fig. 1Aii). The curvatures and shapes of the formed

precurved wings can be tuned by S as discussed later in Fig. 2. Pneumatic actuation of the soft body overcomes the energy barrier (ΔE) in the bistable wings (Fig. 1B) and triggers their simultaneous and quick flexion. Snapping back and forth generates a flapping-wing mode (Fig. 1Aii and movie S1). The formation of the bistable precurved soft actuator and its pneumatic actuated flapping motion are well captured by the corresponding finite element analysis (FEA) simulation (Fig. 2Aiii and movie S1; see Materials and Methods for details).

Similarly, this bistable design can be further extended to a multistable design. Two soft pneumatic bending actuators are connected in parallel and bonded by an H-shaped polyester ribbon frame in the middle (Fig. 1Ci) to form a multistable structure. It allows four different stable buckled shapes in the two wings from stable states I to IV, as shown in Fig. 1Cii (fig. S3A shows the prototype). Figure 1D shows the schematic three-dimensional (3D) energy
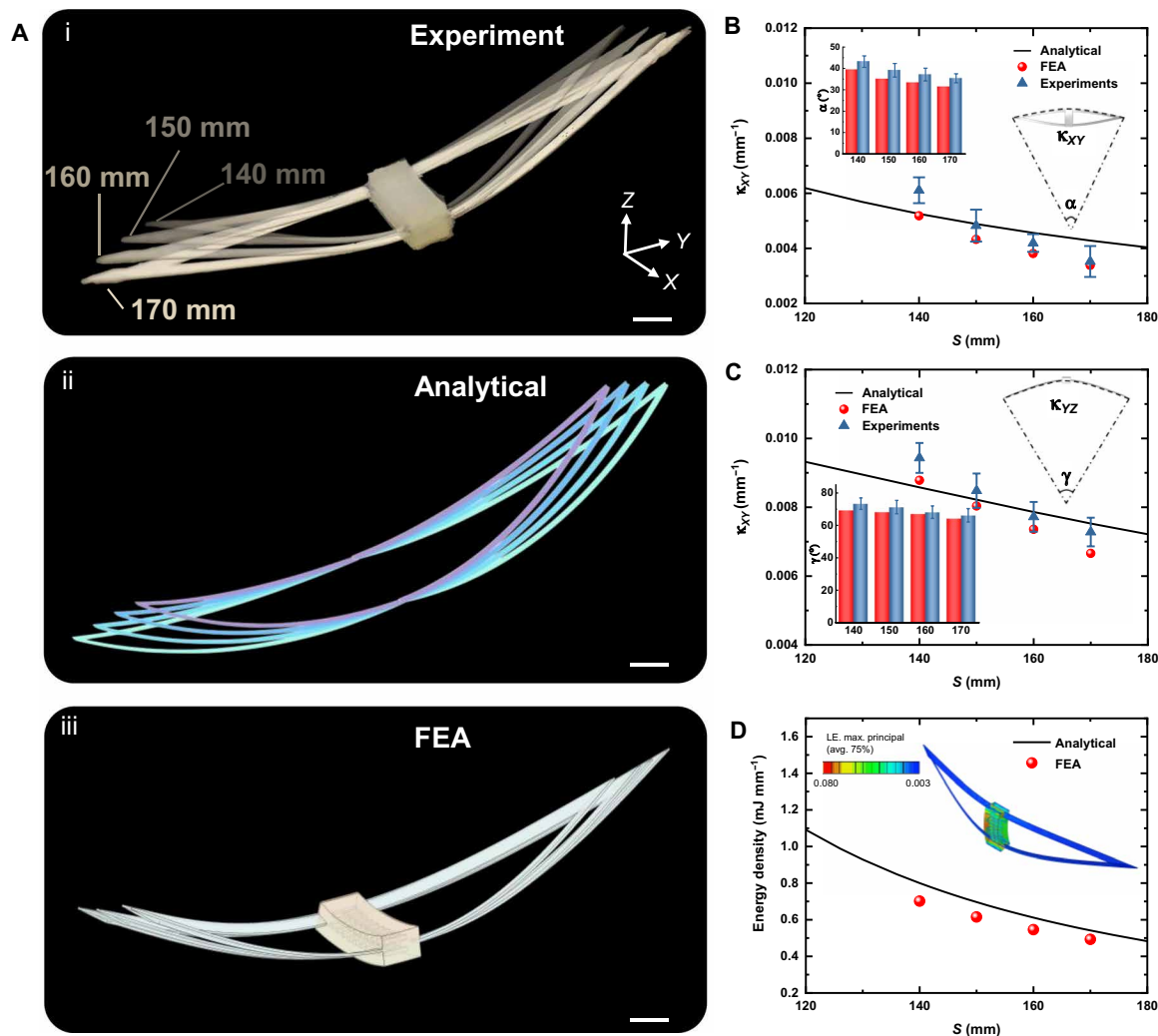
Fig. 2. Tunable precurved shapes in the bistable soft flapping actuators by different wingspan length S. (**A**) The overlapping images of the precurved bistable wings with different S ranging from 140 to 170 mm obtained from experiments (i), finite element analysis (FEA) simulation (ii), and theoretical prediction (iii). Scale bars, 10 mm. (**B** and **C**) Changes of the bending curvatures (κ_{XY} and κ_{YZ}) and bending angles (α and γ) of the bistable flexible ribbons with S from experiments, theory, and FEA simulation; κ_{XY} and α in the XY plane (B); and κ_{YZ} and γ in the YZ plane (C). The right insets show the schematics of the bending curvature and related bending angle. The left insets show the measured bending angle change with S. (**D**) Comparison of elastic energy density of the bistable wings versus S between the theory and FEA simulation. The inset shows the simulated maximum principal strain contour of the bistable wing with $S = 150$ mm.

landscape of the multistable structure, which exhibits one peak in the center (unstable state) and four neighboring localized minimum wells that correspond to the four different stable shapes in Fig. 1Cii. The flapping of either bistable wing can be independently actuated; thus, it can switch between these four combinatorial stable shapes (movie S2). For example, single actuation of either wing will break the symmetric deformation in the pair of wings, i.e., the blue colored loop in Fig. 1Cii, for potential turning and navigation applications as discussed later. Simultaneous actuations of both soft actuators will flip their wing shapes, i.e., the diagonal switch in orange arrows in Fig. 1Cii. To be noted, the energy barrier ΔE_2 for dual actuation mode is twice of single actuation mode ΔE_1, i.e., $\Delta E_2 = 2\Delta E_1$ (Fig. 1D).

On the basis of the proposed designs of the bistable and multistable soft flapping actuators in Fig. 1, in the following, we will first explore the underlying mechanism governing the precurved wing

shape formation in the soft actuators. Then, we will explore their potential amplified dynamic actuation performances by the snapping. On the basis of the understanding of both shape formation and dynamic actuation performances, we will further explore their integration for potential applications in high-speed, high-efficient, bistable, and multistable soft flapping-wing swimmers.

Tunable precurved shapes of the bistable wing

Because the wingspan length S (Fig. 1A) plays a dominant role in determining not only the prestored strain energy but also the thrust force during swimming, we first explore the effect of S on the precurved wing shapes and their bistable performances through combined experiments (Fig. 2Ai), analytical modeling (Fig. 2Aii), and FEA simulation (Fig. 2Aiii). S is selected to vary from 140 to 170 mm for better actuation performances, as discussed later with all the other geometrical parameters remaining the same.

Figure 2Ai shows that the overlapping experimental images of the formed precured bistable wing frames upon bonding the tips of wings with different S. The wing frame becomes bended in both XY and YZ planes because of the tip bonding–induced distortion. Their precured wing shapes can be characterized by two bending curvatures, i.e., κ_{XY} (or bending angle α; inset of Fig. 2B) in the XY plane and κ_{YZ} (or bending angle γ; inset of Fig. 2C) in the YZ plane. Here, we assume uniform curvatures in both planes due to its large aspect ratio S/L (~6.1 to 7.5, with L being the body length and also the distance between parallel ribbons in Fig. 1A) and small maximum principal strain (~0.3% for $S = 150$ mm from the FEA simulation; inset of Fig. 2D) along the ribbons. Figure 2 (B and C) shows that both measured bending curvatures decrease monotonically with the increase of S. As expected, the shorter the wingspan length, the higher prestress and larger curvature it generates and the larger bending stiffness it has (fig. S4A). Equivalently, as S increases from 140 to 170 mm, the bending angles α and γ reduce from ~43.2° to ~35.4° and from ~73.4° to ~66.2°, respectively. Compared to κ_{YZ}, S has a more prominent effect on κ_{XY}. The corresponding FEA simulation results agree well with the experiments as shown in Fig. 2 (Aiii, B, and C).

To better understand the effect of wingspan length S on the buckled precured wing shape, we develop an analytical model to predict its wing shape by minimizing the total elastic strain energy stored in the system (see Materials and Methods for details). Figure 2D shows the theoretically predicted strain energy density u as a function of S. It shows that, as S increases from 120 to 180 mm, u decreases nonlinearly by over a half from about 1.09 to 0.48 mJ/mm, which is consistent with the corresponding FEA simulation results. The higher strain energy density at smaller S also indicates the higher-energy barrier, as evidenced by the enclosed larger area of the force-deflection curves of the bistable actuators in fig. S4A. We further compare the theoretically predicted two curvatures κ_{XY} and κ_{YZ} and the 3D geometric shapes of the buckled wings at different S with experiments, which shows good agreement with each other [Fig. 2, A (i and ii), B, and C].

In addition to S, as shown in the analytical model, the precured wing shape can also be tuned by the dimension of the soft bending actuator L as well as the bending stiffness of the ribbon determined by its Young's modulus and geometry (e.g., the aspect ratio of ribbon cross section, i.e., the ratio of ribbon width w_r to thickness h_r, w_r/h_r). For example, fig. S5 (A to C) shows that, when the wingspan length S is fixed, increasing the body length L of the soft bending actuator leads to an increased bending curvature and bending stiffness as well as a higher critical snapping force; i.e., increasing L is similar to the effect of reducing S. Differently, increasing w_r/h_r barely changes the precured wing shapes (fig. S5D), whereas it leads to a higher critical snapping force (fig. S5E) due to the increased bending rigidity. Thus, geometrically, the larger the ratio of L/S in the flapping soft actuator, the larger curvature and prestored energy it will generate. It should be noted that the potential higher snapping power for soft flapping actuators with a larger L/S or w_r/h_r also correspond to a higher-energy barrier for the actuation inputs to overcome as discussed later.

Figure-of-eight flapping wing and amplified dynamic actuation performances

We further explore the dynamic snapping behavior of the bistable soft flapping actuator upon pneumatic actuation with one end being clamped. Figure 3A shows the representative nine states of the actuator ($S = 150$ mm) in both time-lapse side view and front views, which are captured by a high-speed camera during one downstroke (snap through) and upstroke (snapback) cycle (see Materials and Methods for details and movie S3). The actuation pressure is 55 kPa, and the actuation frequency is 0.714 Hz (see table S1 for the actuation details). The wing tip, curved end of the soft body, and center of mass (CoM) are highlighted in orange, cyan, and red dots as motion trackers, respectively.

Figure 3A shows that the pneumatic actuated bending and slightly elongation deformation in the soft body drive concurrent amplified clockwise rotation and flapping of both wings via snapping. This is in sharp contrast to conventional soft flapping or oscillation actuators that only undergo bending rather than combined bending and rotation here (5–8, 10, 25). Consequently, it results in an interesting figure-of-eight close-looped trajectory of the wing tip in XZ plane during one cycle of downstroke and upstroke wing motions (Fig. 3B). This is similar to the flapping wings observed in a hovering hummingbird and bumblebee to generate an augmented thrust force (Fig. 3, C and D) (27, 28). Differently, the cross shape is steep, representing the snapping through from states ii to iii (within 40 ms) during downstroke and the snapping back from states vi to vii (within 36 ms) during upstroke in Fig. 3A. During snapping, it can achieve an instantaneous peak high tip speed of $v_{\max-x} \approx v_{\max-z}$ ~6.6 m/s ($v_{\max-y}$ ~3.2 m/s) (fig. S6A) and a high instantaneous rate of acceleration $a_{\max-x} \approx a_{\max-z} \approx 1.49 \times 10^3$ m/s^2 ($a_{\max-y} \approx 1.39 \times 10^3$ m/s^2) that is orders of magnitude higher than the gravitational acceleration (fig. S6C), demonstrating a largely amplified dynamic performance. Following the snapping, vibration and damping occur, which will be largely suppressed during swimming as shown later (movie S4). We note that, different from the reported bioinspired flapping mechanism (29, 30), our bistable flapping motion does not need the rigid multiple bar-linkage system between the actuator and the wing (29, 30) to realize the sophisticated figure-of-eight trajectory in the flapping wing.

Snapping can largely amplify both rotating and flapping motion of the wings through sudden release of the stored strain energy, whereas it only requires relatively small bending deformation in the soft body with low actuation energy. To better understand the connection between the pneumatic actuated deformation in the soft body and the induced amplified flapping behavior in the wing, we track the bending angle φ_{body} and deflection d_{body} of the soft body as a function of the actuation pressure as shown in Fig. 3 (F and G, respectively) as well as the corresponding changes in the rotation angle φ_{wing} (Fig. 3H), flapping angle θ_{wing} (Fig. 3I), and deflection d_{wing} of the wing (Fig. 3B). Figure 3E shows the definitions of all the angles and deflections.

Upon inflating the top chamber, i.e., downstroke from states i to ii before snapping, the soft body bends downward with its bending angle φ_{body} decreasing approximately linearly from 10° to approximately −20° with the pressure, i.e., $\Delta^{i-ii}\varphi_{body}$ of approximately −30° (Fig. 3F). Equivalently, its deflection d_{body} decreases linearly from 2.5 to approximately −7.2 mm, i.e., $\Delta^{i-ii}d_{body}$ of approximately −9.7 mm (Fig. 3G). Correspondingly, for the wings, its rotation angle φ_{wing} decreases linearly from 75° to ~40°, i.e., $\Delta^{i-ii}\varphi_{wing}$ of approximately −35° (Fig. 3H), whereas its flapping angle θ_{wing} remains almost unchanged as ~20°, i.e., $\Delta^{i-ii}\theta_{wing}$ of approximately −1° (Fig. 3I), and its deflection decreases slightly with $\Delta^{i-ii}d_{wing}$ of approximately −9.7 mm.
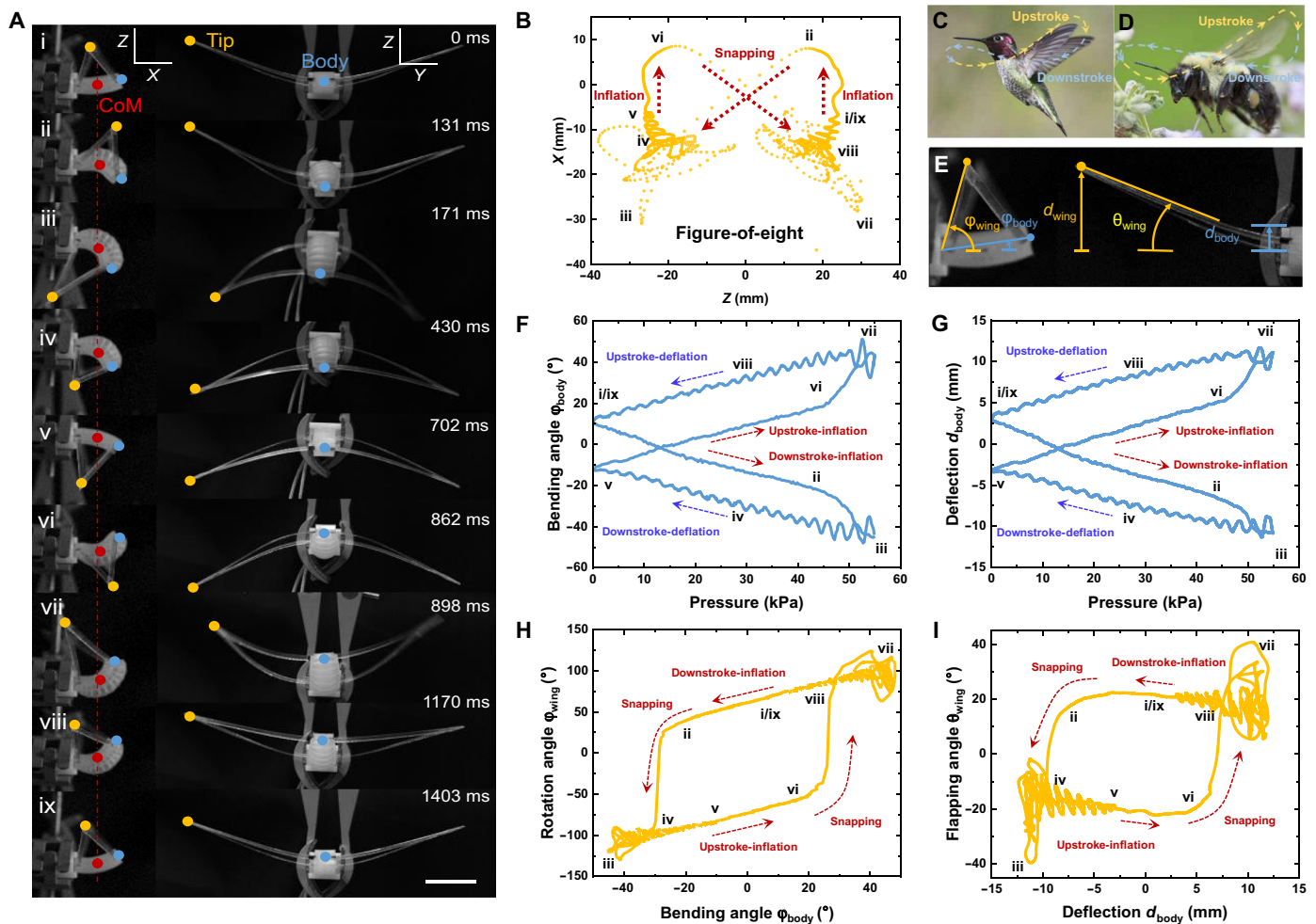
Fig. 3. Snapping-induced amplified flapping and rotating motions in the bistable precurved soft flapping actuator (S = 150 mm). (**A**) The time-lapse images of pneumatic actuated motions during a representative cycle of downstroke [snap-through, states ii and iii in (A)] and upstroke [snap-back, states vi and vii in (A)] wing flapping in both side view (left, *XZ* plane) and front view (right, *YZ* plane) captured by a high-speed camera. The orange and cyan dots denote the wing tip and soft body as motion trackers. The red dot denotes the center of mass (CoM) of the soft body. Scale bar, 20 mm. (**B** to **D**) Trajectory of the wing tip in *XZ* plane follows a figure-of-eight–like loop (B), similar to that of the hovering of a hummingbird (C) and bumblebee (D) at their wing tips. Photo credit: Pixabay (C and D). (**E**) Definitions of soft body bending angle φ_{body} and wing rotating angle φ_{wing} (left), wing deflection d_{wing} and flapping angle θ_{wing}, and soft body deflection d_{body} (right). (**F** to **I**) The bending, rotating, and deflection performances of the flapping actuator. i to ix represent the nine representative dynamic deformed states shown in (A). (F and G) Soft body bending angle φ_{body} and deflection d_{body} as a function of pneumatic pressure p. (H) Wing rotation angle φ_{wing} as a function of φ_{body}. (I) Wing flapping angle θ_{wing} as a function of d_{body}.

During the snapping through from states ii to iii, we note that the relatively small deformation in the soft body can trigger marked and large amplified deformation in the wing. Compared to the deformation before snapping, snapping induces about 4.9 times increase in the wing's rotation angle change (i.e., approximately −170° versus approximately −35° in Fig. 3H), over 60 times increase in the flapping angle change (i.e., approximately −60° versus approximately −1° in Fig. 3I), and about four times increase in the wing deflection change (i.e., −38.8 mm versus −9.7 mm in Fig. 3G). Similar snapping-induced large amplified effects are also observed during the upstroke of the wing from states vi to vii in Fig. 3 (B and G to I). The large amplifying effect is mainly attributed to the millisecond time scale of the dynamic snapping process (*14*, *15*), accompanied by the exponential increase of acceleration to be discussed in Fig. 4. To be noted, because of high-speed snapping, the dynamic inertia effect induces the oscillation of the flexible wing after it

bypasses the equilibrium states, which is also coupled with the decreasing of the pressure as shown in Fig. 3 (F and G).

Effects of the wingspan length *S* on the amplified dynamic actuated performances

Figure 4 (A and B) shows the trajectories of the wing tips of the bistable flapping actuators with their wingspan length *S* varying from 140 to 170 mm in the front and side views, respectively. All the actuation pressure and frequency are kept the same as 55 kPa and 0.714 Hz. The front view (*YZ* plane) shows that the bending motions of all the wing tips follow a similar symmetric arc-shaped path during the upstroke and downstroke motions. The bistable wings exhibit a similar large flapping angle θ_{wing} of ~42°, which is more than 16 times larger than its stable counterpart (θ_{wing} ~2.8°) with flattened, stress-free wings, and more than 8 times larger than that of the reported dielectric actuated stable flapping-wing–based soft

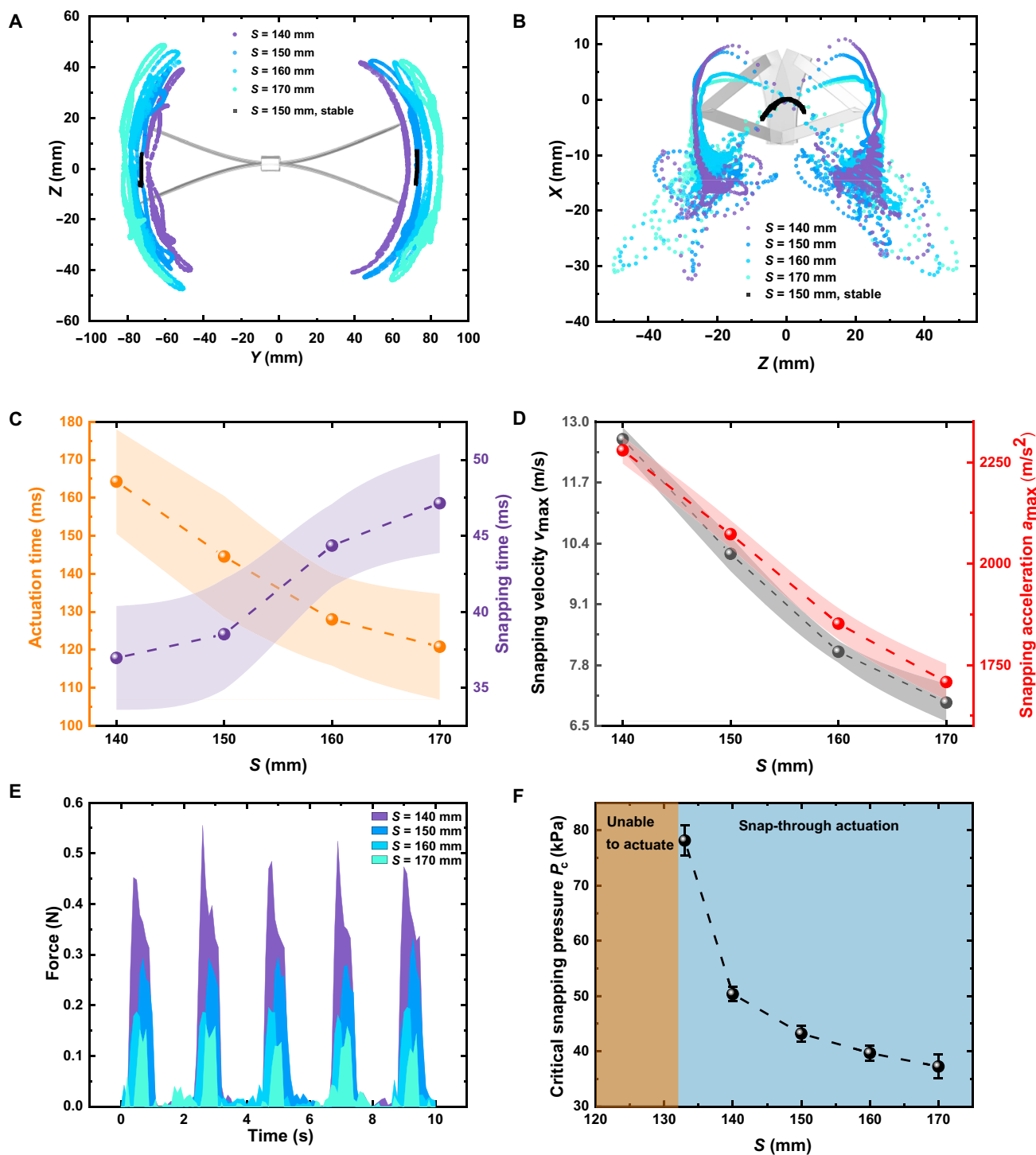**Fig. 4. Comparison of the amplified dynamic performances in the bistable soft flapping actuators with different wingspan length _S_.** (**A** and **B**) Trajectories of the wing tips in _YZ_ plane [front view of two wing tips (A)] and _XZ_ plane [side view of one wing tip (B)] during one downstroke and upstroke flapping cycle in both bistable and stable (denoted by black curves) soft flapping actuators. (**C**) The actuation time and snapping time versus _S_. All actuators are pressurized at 55 kPa with the same flow rate of 1.2 liters/min. (**D**) The maximum instantaneous velocity and acceleration versus _S_ at the onset of snapping. (**E**) The dynamic block force changes with time during actuation. (**F**) The critical snapping pressure to trigger the onset of snapping versus _S_. The gold region denotes the failure in activating the snapping (_S_ < 132.5 mm); beyond that, the blue region denotes the activation zone.

electronic fish (θ_{wing} ~5°) (*31*), indicating the benefit of bistable wing design in the large flapping angle amplification. The trajectories in side view (*XZ* plane) show that all the bistable flapping wing tips follow a similar large figure-of-eight–like profile. In contrast, their stable counterpart shows a small-angled segmental arch shape (black curve in Fig. 4B). The observed oscillated trajectory paths shown on the bottom is due to the vibration and damping after snapping.

We further exploit the effect of the wingspan length *S* on the dynamic and actuation performances of the bistable flapping soft actuators, including the stroke time and snapping time (Fig. 4C), the wing tip's snapping velocity and acceleration rate (Fig. 4D), the dynamic block force (Fig. 4E; see Materials and Methods and fig. S7 for details), and the critical actuation pressure for triggering snap-through instabilities (Fig. 4F). In general, the shorter the wingspan is, the longer actuation time and the faster snapping duration it takes; the higher the snapping speed, snapping acceleration rate, and dynamic blocking force it generates, the higher critical actuation pressure it requires to induce snapping as described below.

Figure 4C shows that as *S* decreases from 170 to 140 mm, it takes a longer actuation time t_{actn} to reach the onset of snapping under the same amount of energy input, i.e., t_{actn} increases from ~120 to ~164 ms, attributing to the higher bending stiffness resistance and energy barrier in the shorter wingspan (fig. S4). By contrast, it snaps faster with snapping time t_{snap} reducing from ~47 to ~37 ms. This is due to the faster energy release of the higher strain energy stored in the shorter wingspan *S*, where both snapping velocity v_{max} and acceleration rate a_{max} increase with decreasing *S* as shown in Fig. 4D. For example, when *S* shortens from 170 to 140 mm, v_{max} increases from ~7.0 to ~12.6 m/s and a_{max} increases from ~2106 to ~2764 m/s^2. Correspondingly, the peak dynamic block force is largely enhanced by more than threefold, where it increases from ~0.15 N at *S* = 170 mm to ~0.52 N at *S* = 140 mm, as shown in Fig. 4E.

Meanwhile, the achieved amplified force at shorter *S* also requires an applied higher critical actuation pneumatic pressure P_c to trigger the snap-through by overcoming the higher-energy barrier as shown in Fig. 4F. As *S* reduces to below 140 mm, P_c increases steeply from ~50 kPa at *S* = 140 mm to ~78 kPa at *S* = 132.5 mm. This length also corresponds to the critical wingspan length S_c for the current design, below which the pneumatic soft body fails to activate the snapping of the bistable wings even when it is overinflated (more than 120 kPa) because of its markedly increased energy barrier (fig. S8).

Butterfly stroke–like, high-speed soft flapping swimmer

Next, we explore harnessing the bistable flapping soft actuators for potential applications in fast-speed and high-efficient swimming soft robots. As schematically illustrated in Fig. 5A, the soft swimmer is constructed from simply covering the wings of the flapping soft actuator with a flexible membrane, alongside two flexible film-based extended fins attached to the trailing edges of both wings for amplifying the propulsion (see Materials and Methods for details).

Figure 5B and movie S5 show the side view of its swimming performance at the water-air interface (*S* = 150 mm, actuation pressure is 55 kPa, and frequency is 0.625 Hz). Initially, at *t* = 0 s, the floating swimmer is fully immersed in water except the upward wing tips and its body is angled slightly. Upon inflating the top pneumatic chamber, the soft body starts to bend downward (convex shape). However, it barely moves forward. When beyond the onset of snapping at *t* = 0.225 s, two wings start to simultaneously flap

(downstroke motion) and rotate within a short snapping duration of about 46 ms (from *t* = 0.225 s to *t* = 0.271 s). Consequently, it pushes water downward alongside the inflation-induced buoyancy to lift the body close to the water surface (*t* = 0.271 s). Meanwhile, it creates vortices behind (movie S6) and pushes water backward to generate the thrust force and propel it forward. The body shows an angled posture with its head diving into the water (*t* = 0.817 s).

Upon inflating the bottom pneumatic chamber to bend the soft body upward (concave shape), it induces the snapping back of both wings. Notably, the fast upstroke and rotating motion of the wings push the soft body against the buoyancy and make the body steeply dive into the water (*t* = 1.073 s), propelling it forward with its head floating up (*t* = 1.285 s). The swimmer recovers to its initial posture with two tips floating on water upon deflation of the bottom chamber (*t* = 1.614 s).

We find that its swimming postures are similar to the most challenging butterfly swimming stroke in humans (insets of Fig. 5B) that gets its name from its sweeping arm action reminiscent of a butterfly's wings (*32*) in terms of the body and arm motions. The inset of Fig. 5A shows the butterfly swimming stroke of an athlete with the laterally extension of his arm to maximize the thrust force. During the butterfly stroke, the human body undergoes undulating motion with the head, leading the movement of the stroke. The wing-like arms provide most of the propulsion for the stroke by simultaneously stretching out, pulling, and sweeping both arms for propulsion (*33, 34*). Similarly, our soft swimmer bends its soft body to generate a wave-like undulation with its head moving up and down during the stroke, as shown in the tracked undulating trajectory of its soft body mass center in Fig. 5C. The undulating soft body coordinates with the simultaneously fast strokes of flapping and sweeping of both flexible wings via rotation for propulsion. Differently, during the recovery phase of the butterfly swimming stroke, the upstroke wing action in our swimmer can also provide thrust force to swim forward. Such a burst swimming mode is further verified by monitoring the instantaneous velocity changes during swimming as shown in Fig. 5D. The swimming motion is accelerated by the snapping of the wings, which shows a peak instantaneous high swimming speed of ~0.45 m/s during the snapping of downstroke. Then, it reduces to a slow swimming velocity of ~0.05 m/s after finishing the downstroke.

Fast and lower–energy cost swimming performances

Next, we further explore the effects of wingspan length *S* and actuation frequency *f* on its swimming performance at the water-air interface (Fig. 6, A and B, and movie S7) under the same pressure of 55 kPa. Figure 6A and movie S7 show the comparison of their swimming performances for the bistable flapping-wing swimming robots with *S* varying from 140 to 170 mm under the same *f* = 0.67 Hz. It shows that the swimmer with an intermediate *S* = 150 mm swims the fastest, as also observed under different actuation frequencies (Fig. 6B), where their swimming speeds increase with *f*. The highest speed observed in the case of an intermediate *S* = 150 mm can be qualitatively explained as follows. As discussed above, the bistable swimmer with a shorter *S* has a higher prestored stain energy in its precurved wings. Thus, generally, it can generate a higher hydrodynamic flapping force for propulsion upon snapping-induced larger energy release. However, the higher flapping force is compromised by its relatively shorter wingspan length, which consequently results in a smaller interaction surface area with fluids (fig. S9) to lower its
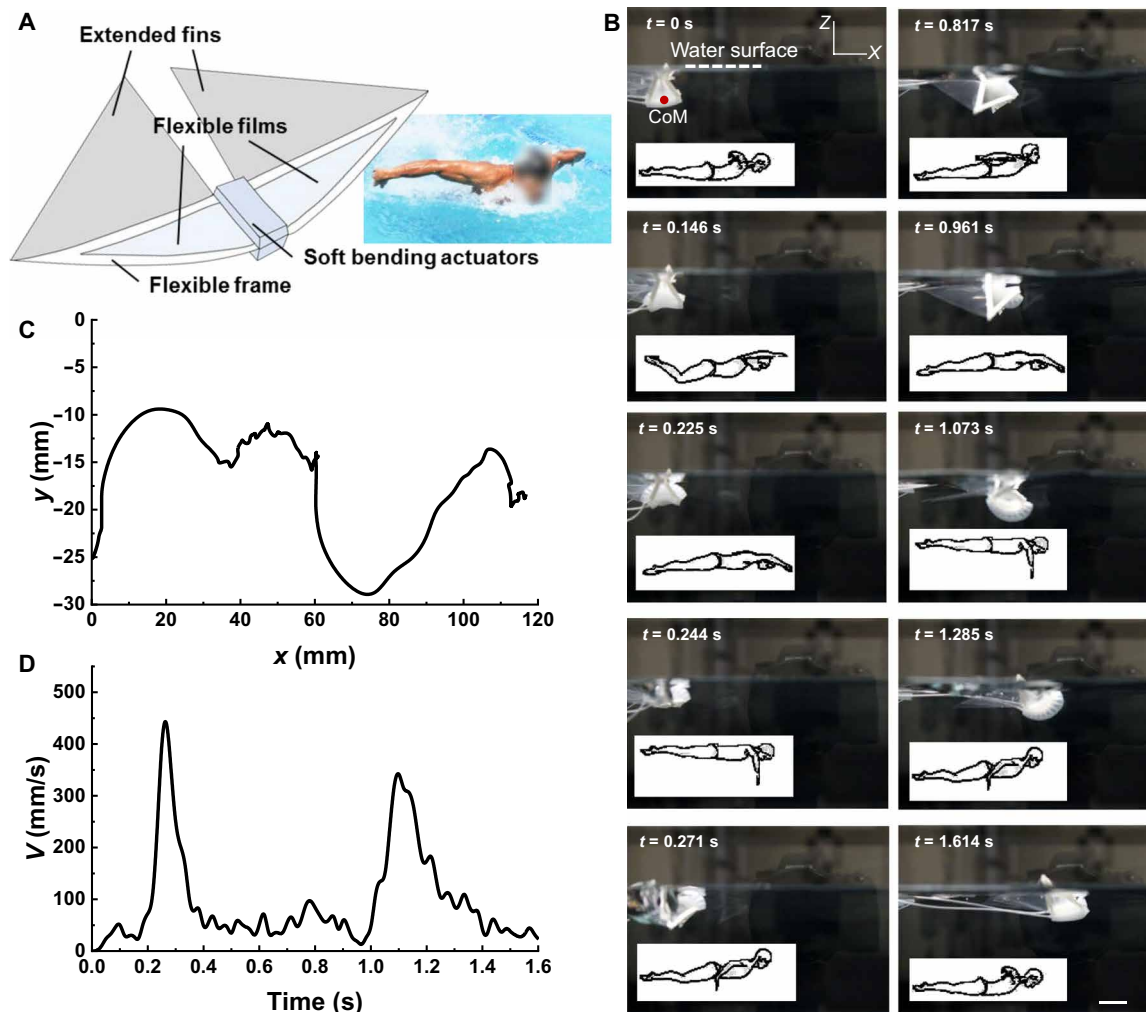
Fig. 5. Butterfly stroke–like bistable flapping-wing soft swimming robot. (**A**) Schematic of the proposed bistable soft swimming robot by attaching the bistable flapping soft actuator with flexible films and extended fins. The inset shows the butterfly swimming stroke. Photo credit: Pixabay (inset). (**B**) The time-lapse side-view images of the representative swimming gaits in the bistable swimmer with a wingspan length of $S = 150$ mm during one cycle of down- and upstroke under an actuation pressure of 55 kPa and a frequency of 0.625 Hz. The insets show the schematic human's swimming postures of the butterfly swimming stroke (*32*). Reproduced with permission (*32*). Copyright 1999, Elsevier. Scale bar, 15 mm. At $t = 0$ s, the floating swimmer is fully immersed in water except the wing tips with its wings flapped upward and body angled slightly. Upon inflating, the body starts to bend downward and barely moves forward until beyond the onset of snapping at $t = 0.225$ s, two wings quickly and simultaneously stroke downward and rotate within 46 ms (from $t = 0.225$ s to $t = 0.271$ s). Consequently, it lifts the body close to the water surface ($t = 0.271$ s) and propels forward. The body shows an angled posture with its head diving into the water ($t = 0.817$ s). Upon inflating to bend the body upward to snapping both wings back, the fast wing upstroke and rotation make the body steeply dive into the water ($t = 1.073$ s), propelling it forward with its head floating up ($t = 1.285$ s). The swimmer recovers to its initial posture at $t = 1.614$ s. (**C**) The tracked CoM motion of its soft body. (**D**) The velocity profile of the bistable butterfly stroke–like soft swimmer.

thrust force and swimming speed (*35*). Similarly, for the swimmer with a longer wingspan length, they have larger interaction surface areas whereas generate a smaller flapping force for propulsion due to the lower prestored energy. Such qualitative explanations are further validated by the observed maximum peak thrust force for the case of $S = 150$ mm, where the measured peak thrust force increases first and then decreases as S increases from 140 to 170 mm (fig. S10B). We note that, unlike the fast bistable swimmers, their stable counterpart ($S = 150$ mm) can barely move because of its nonamplified, much smaller flapping and rotation angles (Fig. 4, A and B, and movie S8). Such intermittent swimming or burst-and-coast swimming style can generate higher thrust force for fast swimming speed than the undulating swimming mode at low-frequency domain

(*36*). After parametric studies, we find that the bistable soft swimmer with $S = 150$ mm actuated at 55 kPa and 1 Hz achieves the maximum fast speed of 85.27 mm/s, which corresponds to 3.74 BL/s (orange star in Fig. 6B and movie S9).

Similar to the effect of S on the swimming speed, the fastest soft swimmer with an intermediate $S = 150$ mm also shows the lowest cost of transport (CoT) that quantifies the energy efficiency (Fig. 6C). $\text{CoT} = E/(m \times g \times d)$ is to quantify and evaluate the energy consumption of transporting a target object with a certain distance, where E is the energy input to the system, m is the mass, g is the standard gravity, and d is the moved distance. Lower CoT indicates lower energy consumption. The energy input of the system mainly comes from the electrical power to supply the pneumatic pump
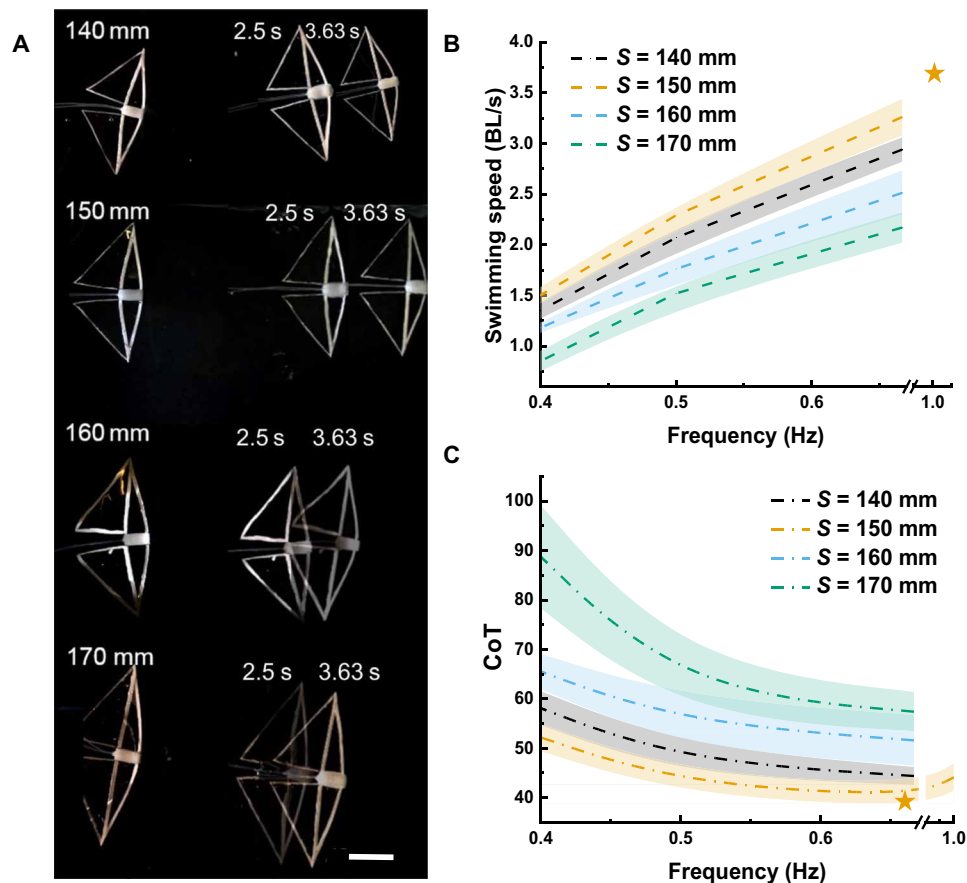
Fig. 6. Bistable soft flapping-wing swimmers with both higher speed and lower energy cost. (**A**) Comparison of the swimming performance between the bistable swimmers with different S in top view of the overlapping time-lapse images. All actuators are pressurized at the same pressure of 55 kPa and actuated at the same frequency of 0.67 Hz. The swimmer with $S = 150$ mm shows the fastest speed (~ 3.4 BL/s, 0.67 Hz). Scale bar, 40 mm. (**B** and **C**) The relative speed and cost of transport (CoT) of the bistable soft swimmers with different S as a function of actuation frequencies. The orange star shows the fastest swimming speed (3.74 BL/s) for the swimmer with $S = 150$ mm under 1-Hz actuation frequency. The swimmers with $S = 150$ mm shows both the fastest speed and the lowest CoT.

(3 V, 0.12A). We plot the relationship between the actuation frequency f (double the frequency of the electrical power supply) and CoT for the soft bistable swimmers with different S as shown in Fig. 6C. For the frequency range of 0.4 to 0.67 Hz, the CoT decreases with the increasing f for different S. The fastest soft swimmer with an intermediate $S = 150$ mm shows the lowest CoT. However, as f further increases to 1 Hz, its CoT also increases slightly, showing a U-shaped CoT curve with f (Fig. 6C). The lowest CoT of ~39 is achieved at f ~ 0.67 Hz with a high speed of 3.4 BL/s.

Comparable fast and high-efficient swimming performances to biological counterparts

We further compare the swimming performance of our high-speed bistable soft flapping-wing swimmer ($S = 150$ mm) with the reported fast-swimming soft robots (5–8, 10, 22–26) and several speedy biological swimmers in wildlife (37–44) with similar flapping or wave-like motions for propulsion (45) by categorizing them in a diagram of relative speed (body length per second) versus body mass in Fig. 7A. We note that the speed of the reported stable soft swimmers with similar flapping or wave-like motions for propulsion is entangled below ~1 BL/s (0.01 to 0.69 BL/s) (6–8, 10, 22–26). Despite the reported higher swimming speed than 1 BL/s in soft robotic swimmers (46, 47), they are not included in Fig. 7A for

comparison because of their distinct propulsion mechanisms such as water jetting (46) and propellers (47). Compared to the fastest speed (0.78 BL/s) of our reported bistable fish-like soft swimmer that harnesses swing body motion (5), the bistable soft flapping-wing swimmer here can achieve 4.8 times faster speed (3.74 BL/s) under much lower actuation pressure (55 kPa versus 160 kPa) with more than 18 times lighter weight (a mass of 2.8 g versus 51 g). Amplified by the bistability and butterfly-like swimming posture, the relative swimming speed of our soft swimmer (1.5 to 3.74 BL/s) is even faster or comparable to some of the marine animals such as manta rays (~1.73 BL/s), dolphins (~3.28 BL/s), and Humboldt penguins (~4.50 BL/s) (Fig. 7A).

Figure 7B further plots the propulsion efficiency of the fast-speed, bistable soft flapping-wing swimmers in terms of St as a function of the actuation frequency f. We find that, except the case of $S = 170$ mm actuated at 0.4 Hz, St of all the studied bistable swimmers here fall within the observed naturally selected narrow range of $0.2 < \text{St} < 0.4$ (two parallel dash lines in Fig. 7B) in biological swimmers for the maximum propulsion efficiency (3, 4). It indicates that our soft swimmers can achieve both a high speed (3.4 to 3.67 BL/s) and a high propulsion efficiency ($0.2 \leq \text{St} \leq 0.255$). In contrast, St of the reported flapping or oscillating-based soft swimming robots in literature are either well above the upper bound or below the
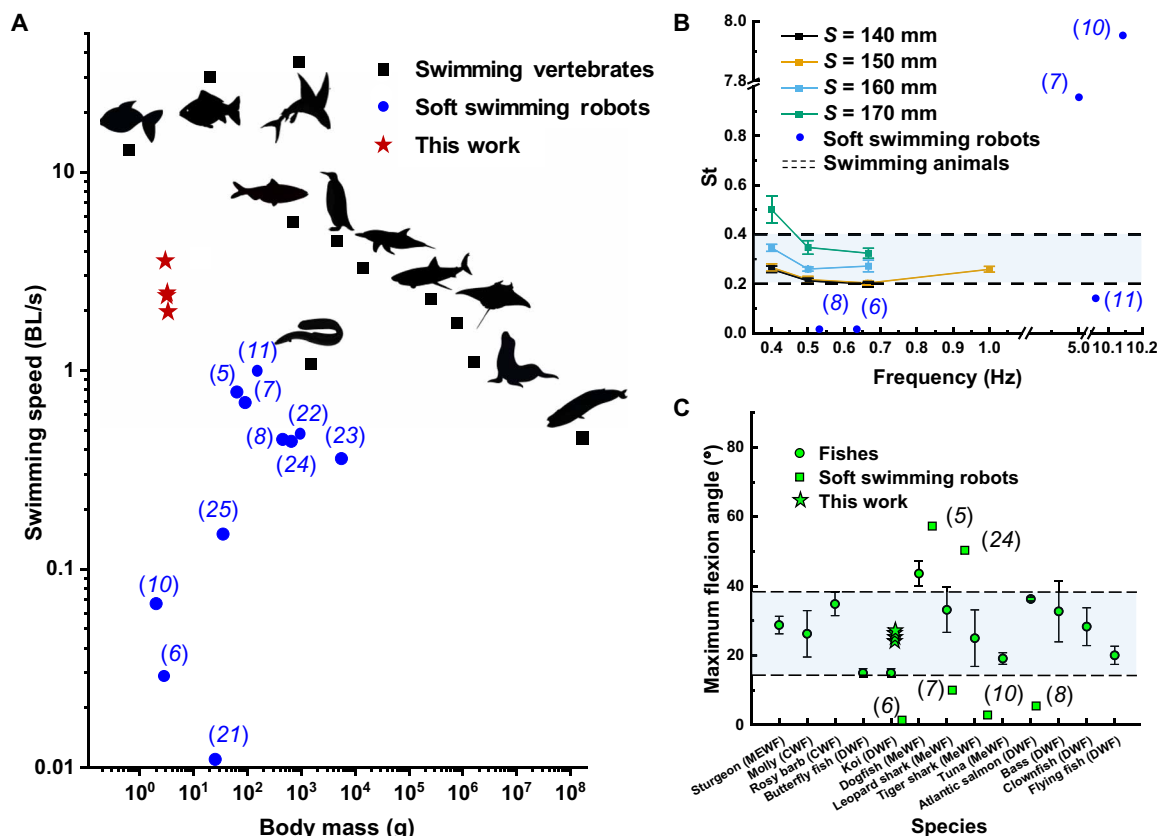
Fig. 7. The high-speed and high-efficient bistable flapping-wing soft swimming robots (S = 150 mm) with comparable performances to their biological counterparts. (**A**) Comparison of the swimming speed (body length per second) versus body mass between the proposed high-speed bistable flapping soft swimmers (red stars, mass of 2.8 g, S = 150 mm at frequencies from 0.4 to 1 Hz), some marine vertebrates, and the reported soft swimming robots in literatures (*5–8*, *10*, *22–26*). (**B**) Comparison of St as a function of actuation frequency between the bistable flapping soft swimmers with different S and the reported soft swimming robots in literatures (*6–8*, *10*, *11*). The two dashed lines define the lower and upper bounds of the observed narrow range of the optimal St (0.2 to 0.4) in swimmers for maximum propulsion efficiency. (**C**) Comparison of the optimal range of maximum wing and fin flexion angles (~15° to ~40°) in fishes (*48*) between the fast-speed bistable flapping soft swimmers (S = 150 mm) and the reported soft swimming robots in literatures (*5–8*, *10*, *25*).

lower bound of the optimal naturally selected range, where the swimming speeds scatter from 0.02 to 0.78 BL/s actuated at a wide low-to-high frequency range of 0.5 to 10.13 Hz (*6–8*, *10*, *11*) (Fig. 7B). Figure 7C shows another convergently optimal narrow range observed in a variety of swimming animal propulsors in terms of the maximum wing and fin flexion angles (~15° to ~40°) for the high efficiency of different swimming animals (*48*). We also find that the maximum flexion or flapping angle of our swimmers (~27°) also falls into the optimal range of its biological counterparts. In contrast, the reported soft swimming robots are either much higher or lower than the maximum flexion angle range (Fig. 7C) (*5–8*, *10*, *25*).

Multistable soft flapping-wing swimmer with enhanced maneuverability

Despite the demonstrated high-performance soft flapping-wing swimmers that are comparable to their biological counterpart in terms of high speed and high efficiency, it can only achieve unidirectional forward swimming. To address the limitation, we further develop a maneuverable flapping-wing swimming robot that is capable of directional turning. As shown in Figs. 1C and 8A, similar to its bistable counterpart, the maneuverable swimmer is constructed from a multistable soft flapping actuator with two soft pneumatic

bending actuators connected in parallel in the middle as the soft body (see Materials and Methods for details). The two bistable wings with wrapped thin films and extended flexible fins can be either independently flapped under single actuation for turning motion or simultaneously flapped under dual actuations for forwarding motion with enhanced maneuverability (Fig. 8, B to D).

Figure 8B shows the overlapping time-lapse images of its navigation path marked by the dashed line (movie S10). Its corresponding control sequence of the pneumatic flow rate is shown in Fig. 8D, where the pulsed amplitude and time for the flow rate are maintained at 1.2 liters/min and 0.172 s, respectively. Starting from a vertically placed posture in state I, upon solely actuated flapping of the left wing, the swimmer rotates clockwise from states I to II, making a right turn, followed by an angled forward motion to state III under dual actuations of both wings. Then, it solely flaps its right wing to turn left to adjust its moving direction (state IV), followed by directional swimming from states IV to V under dual actuation. We note that the multistable soft swimmer can generate a relatively large steering angle of ~25.5°/28.5° (clockwise/counterclockwise) per flapping stroke within 172 ms as shown in the inset of Fig. 8C, which corresponds to a fast turning speed of ~157°/s. Such a speed is even higher than the recently reported fastest turning speed of
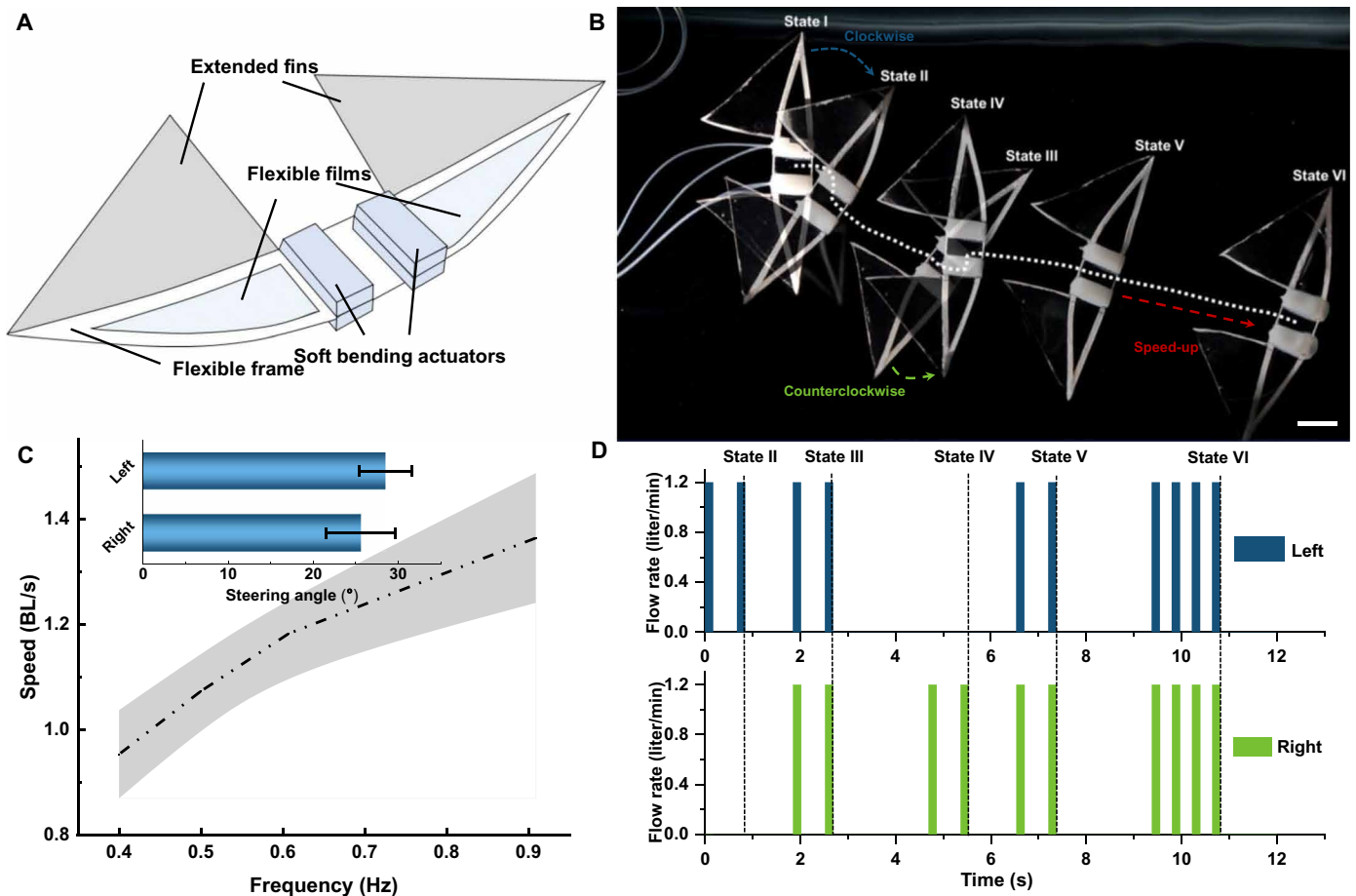
Fig. 8. Multistable soft flapping-wing swimmer with enhanced maneuverability. (**A**) Schematic of the multistable, maneuverable soft swimming robot by attaching the multistable flapping soft actuator with stretchable films and extended fins. (**B**) to (**D**) demonstrated maneuverability (B) with tunable speeds (C) and controllable turning (D). (B) The overlapping time-lapse images of its navigation path through a right turn (state II), directional motion (states II and III), left turn (state IV), and speed-up directional motion (states IV to VI). Scale bar, 20 mm. (C) The variation of relative speed of the multistable soft swimmer with the actuation frequency. The inset shows the steering angles under the single impulse of the flapping motion for the wings. (D) The corresponding actuation control of the flow rate in the left and right pneumatic bending actuator for the navigation path shown in (B).

138.4°/s in the soft dielectric jumping robots on ground (*49*). In addition to the tunable swimming direction, similarly, its swimming speed can also be manipulated and accelerated by increasing the actuation frequency from 0.54 (states IV to V) to 0.72 Hz (states V to VI) as shown in Fig. 8B and movie S10. As expected, similarly, Fig. 8C shows that its swimming speed increases monotonically with the actuation frequency and can reach ~1.4 BL/s at 0.9 Hz. The compromised speed is due to its increased weight and modified design compared to its bistable counterpart.

DISCUSSION
In this work, we demonstrate harnessing snapping-induced amplified flapping and rotating of bistable and multistable flexible wings for achieving high-speed, high-efficient, and maneuverable swimming performance in a soft robotic swimmer. The achieved high swimming performances fall into the naturally selected optimal narrow design space for high propulsion and energy efficiency and are even comparable to that of their biological counterparts. The generic principle and simple flexible robotic structures presented in this

work could be applied to other electric or stimuli-responsive actuations for small-scale transmission-free flapping-wing robots such as soft aerial robots or micro-air vehicles (MAVs), soft amphibious flying and swimming robots, and other jumping and kicking robots (fig. S11 and movies S11 and S12).

Despite the promising results in this work, the full potential of the generic and scale-independent bistable and multistable flapping-wing mechanism for high performances still remains to be unleashed because of the intrinsic limitations of the soft pneumatic bending actuators such as low energy density and limited bandwidth. It also remains to be explored regarding applying its applications to other actuation mechanisms. These leave ample space for future studies and improvements.

First, achieving even faster swimming speed yet high efficiency is hindered by the low bandwidth of about 1 Hz of the miniaturized pneumatic soft bending actuator. The low actuation frequency is mainly attributed to the small-sized air channels (cross section of 0.8 mm by 1 mm) and air hoses (inner diameter of ~0.5 mm) for relatively slower pressurization/depressurization actuations. Such a low bandwidth largely limits its applications to the scenarios that favor

high frequency such as swimming and flying robots. In principle, for the observed t_{snap} of ~37 ms at $S = 140$ mm, it could potentially allow an upper limit actuation frequency $f_{limit} = 1/(2t_{snap})$ of ~13.5 Hz; thus, the full potential of snap-through instabilities has yet to be realized. The time scale of snapping in the bistable flapping-wing actuator t_{snap} approximately scales with S^2 (13), i.e., $t_{snap} \propto S^2$. Thus, a relatively smaller size of S for allowing higher actuation is favorable. For example, given the observed t_{snap} of ~37 ms at $S = 140$ mm, we expect that, for insect-sized flapping-wing flying robots with S below 20 mm, t_{snap} could be below 0.8 ms for allowing a potentially high actuation frequency of up to 625 Hz. Thus, to achieve the high frequency, soft bending actuators with high bandwidth such as piezoelectric (e.g., polyvinylidene difluoride bimorph structures over 100 Hz) (50) or dielectric actuators (more than 10 Hz) will be preferred (29, 30) and explored in the future for potential applications in miniature soft flying robots and transmission-free flapping-wing MAVs (51). We note that the transmission-free flapping-wing design here could also largely reduce its self-weight by eliminating the complex compliant mechanism-based transmission systems often used in flapping-wing flying robots (29, 30, 51). In addition to the frequency, the critical force F_{cr} from the soft bending actuator that drives the snap-through instabilities in the flexible flapping wing is important. We note that F_{cr} approximately scales with $F_{cr} \propto E_r w_r d_{wing}(h_r/S)^3$ with E_r, w_r, and h_r being the Young's modulus of wing ribbons, wing frame ribbon width, and ribbon thickness, respectively. For the studied flexible flapping-wing structure with $S = 140$ mm, $w_r = 3$ mm, and $h_r = 0.55$ mm, we have F_{cr} of ~0.8 N (fig. S4A). For insect-sized robots with S below 20 mm, to achieve a small critical driving force of below 0.1 N or even 10 mN that matches the scale of dielectric or piezoelectric actuators (29, 30), several means would be expected to take and explored in the future, including reducing w_r and/or h_r or using less stiff yet flexible materials.

Second, the demonstrated fast-speed swimming is still tethered to the air supply. Untethered actuation will be highly desired for achieving autonomous, high-speed soft swimming, jumping, and flying robots. The untethered systems could be achieved by either integrating miniaturized on-board sensing, controls, and power or using remote actuation methods such as light or magnetic field (52–54).

Third, its body and wing shapes could be further optimized by exploring the complex flexible structure-fluid interactions through computer fluidic dynamics simulations and experiments to further increase the swimming speed and efficiency. Fourth, the working zone of the current swimmer is close to the water surface. To achieve underwater swimming, appropriate buoyancy control will be needed by either adding the buoyancy regulator or replacing the pneumatic actuation with hydraulic actuation for future study.

Fifth, the load carrying capability of the swimmer remains to be examined. We expect that the carried load would reduce its effective body length, which will result in a reduced elastic energy density for lowering the snapping strength (fig. S5A) and thus degrade its swimming performance.

MATERIALS AND METHODS
Fabrication and actuation of bistable and multistable soft flapping actuators
The bidirectional pneumatic soft bending actuator was fabricated by following the typical manufacturing technique for fluid-driven soft actuators through molding and demolding approaches as shown

in fig. S1. Ecoflex 00-50 (Smooth-On Inc.) was used as the elastomeric materials for three sections of the soft bending actuator. The molds for two channel layers and intermediate layer were made of VeroWhite and 3D printed by Stratasys, Objet260. Three cured Ecoflex layers were bonded by uncured Ecoflex 00-50. The flexible ribbons (ribbon width, 3 mm) are made of polyester sheets (thickness, 0.55 mm; Grafix) and were laser-cut to desired geometry and embedded into two edges of pneumatic actuator by Smooth-On SIL-Poxy Silicone adhesive; two tips were bonded by Instantbond Adhesive 403 to form the bistable/multistable structures. For experimental characterization of the geometries, dynamic performances, and swimming performances of the bistable soft flapping actuators and soft swimmers with different wingspan lengths ($S = 140, 150, 160,$ and 170 mm), the multistable flapping actuator and swimmer, and the stable counterpart ($S = 150$ mm), triplicated prototypes were fabricated at minimum.

Theoretical modeling of the buckled precurved wing shape
The strain energy density U of the bistable flapping system can be expressed as

$$U = a\kappa_{XY}^2 + b\kappa_{YZ}^2 + (1 + c)\tau^2 \qquad (1)$$

by considering the bending energy in the two planes (the first two terms) and the torsion energy (the third term), where a and b are the rigidity ratios of the wing ribbon with $a = EI_1/GJ$ and $b = EI_2/GJ$. The strain energy in the soft body can be negligible compared to the wings, considering its small bending deformation and much lower modulus. E and G denote the Young's modulus and shear modulus of the ribbon, respectively. I_1, I_2, and GJ are the principal moments of inertia of the cross section of the ribbon and the torsional rigidity, respectively. c is the parameter denoting the energy stored in the actuator due to the twisting of the wing ribbon with τ being the torsion. c is in the form of $c = GJL/E_aI_aS$, where E_a and I_a are the Young's modulus and the principal moments of inertia of the cross section of the actuator. On the basis of the experimental measurements, the curvature and torsion of the wing's ribbon barely changes with the arc length. Thus, we use helical functions to approximate the shape of the wings and the curvature κ and torsion τ, which take the form of

$$\kappa = r/(r^2 + c^2), \tau = c/(r^2 + c^2) \qquad (2)$$

where the parameterization of the curve is expressed as $\tilde{r} = (r\cos t, r\sin t, ct)$. According to the Meusnier's theorem, κ_1 and κ_2 are the projection of κ (45). The constraints are given by $\sqrt{r^2 + c^2}\,t = l$ and $r\cos t \cos\varphi + ct \sin\varphi - r\cos\varphi = w$, where l and w denote the length of the wing ribbon and the half length of the actuator, respectively. φ is the rotation angle of the ribbon about the y axis and barely changes with the varying lengths of the ribbons. Note that we assume that the length of the actuator does not change when there is no air input. By minimizing the elastic energy stored in the system, its buckled wing shapes can be obtained.

Dynamic block force measurement
To quantify the flapping performance of the bistable actuator, we measured the dynamic block forces at the tips for different bistable flapping actuators with varied wingspan length S. The dynamic block force is defined as the impact force at the tips of bonded ribbons when its flapping motion actuated from one equilibrium state is

blocked by a force sensor at another equilibrium state as shown in fig. S7. The actuation pressure is set to 55 kPa, and the actuation frequency is set to 0.5 Hz for measurement. The flapping motion of the actuator generates a succession of impulses where the maximum stroke is determined as dynamic block force.

Force-displacement curves characterization
We characterized the static mechanical response of the bistable soft actuator with precured wings through quasi-static indentation tests using Instron 5944 tensile tester. As schematically shown in the inset of fig. S4, one end of the pneumatic soft bending actuator, i.e., the soft body, was fixed; the other end, i.e., the head of the soft body, was vertically indented under a load control with a loading rate of 5 mm/min. The indentation forces and displacements were recorded and measured to plot the indentation force-displacement curves of the precured soft actuators with different wingspan length S. To characterize the bistable bending behaviors of both wings, a pair of parallel indentation forces with a distance d_m normalized by the projected wingspan length l_w are applied to the two wings (fig. S4), the CoM was fixed, and the flexible ribbons were vertically indented under a load control with a loading rate of 5 mm/min. The indentation forces and displacements were recorded and measured to plot the indentation force-displacement curves of the precured soft actuators with different wingspan length S.

Motion capture
The motions of studied bistable actuators and robots were captured by a high-speed camera (Photron SA-2) with the frame rate of 1000 frames per second. The motions are tracked by the customized markers on both tips of wingspan and analyzed through Photron FASTCAM Analyzer.

Fabrication and actuation of soft swimming, jumping, and kicking robots
For flapping-wing soft swimming robots, based on the fabricated bistable/multistable soft flapping actuators, a stretchable thin film (3M Tegaderm transparent film roll, 16004) was wrapped around the bonded ribbons to form a membrane wing. On the trailing edges of both wings, triangular-shaped flexible films (width, 47.5 mm; Scotch tape) were attached to the two flexible polyester ribbons as extended fins. Small-sized air hoses are used with an inner diameter of 0.508 mm and an outer diameter of 1.194 mm for all the pneumatic actuations. For jumping soft robots, rather than bonding two end tips of the H-shaped flexible polyester ribbons, the two polyester ribbons were bonded at certain distance away from the end tips to form cross-shaped ends to increase the contact region with ground. A low air flow rate of ~20 ml/s was inflated into the top pneumatic chamber of the soft bending actuator with up-flapped wings to slowly bend the soft body (compared to snapping of two wings) and drive the passive snapping of the wings. For kicking soft robots, the fabricated bistable flapping soft actuator with a wingspan length of 140 mm was used as the ball-kicking soft robot. One end of the vertically placed bistable actuator was fixed to a rigid stand, and the actuator was actuated under a pneumatic pressure of 55 kPa. The actuation timing controls for the bistable and multistable actuators, swimmers, jumpers, and kickers are listed in table S1. We follow our previous work on the experimental setup of the pneumatic inflation system for the soft robots and measurements of critical actuation pressure and flow rate for the bistable soft flapping actuators (5).

Aquatic experimental setup
The soft swimmers were place into a 121 cm–by–32.3 cm–by–31.6 cm aquarium and filled with 25 gallons of water. An open-looped pneumatic control system was tethered to the swimmer (55, 56). The swimming processes were filmed using Photron SA-2 (Stationary in-water test) and Canon 6D mark II. White colored light-emitting diode was used as illumination.

Thrust force measurement of the soft flapping swimmers
As illustrated in fig. S10A, the force sensor (Instron, 2530-5N) and a rigid rope are connected to the rear part of the soft swimmer. The soft swimmer is placed into an 18 cm–by–18 cm–by–18 cm aquarium and filled with 1 gallon of water. The thrust force is determined as the difference of force peak and base load during swimming of the soft swimmer (actuation frequency, 0.67 Hz). The average thrust force generated during five cycles of snapping is reported in fig. S10B.

FEA simulation of bistable and multistable flapping actuators
Parametric FEA simulation studies were conducted to investigate the formation of the precured bistable and multistable actuators by bonding the tips with different wingspan length as well as their actuated snapping-induced flapping performances under pneumatic actuations. The 3D geometric models of the H-shaped soft flapping actuators before bonding were built using the SolidWorks software with the same measured geometrical dimensions as the prototypes. The commercial FEA software Abaqus was used for the FEA analysis with the Abaqus/Standard solver. The built geometric models of all the actuators in SolidWorks were imported into Abaqus CAE as STL files and were meshed using the solid quadratic tetrahedral elements (C3D10). A mesh refinement study was conducted to verify the accuracy and convergence of the mesh. The flexible polyester ribbons are modeled with linear elastic materials with Young's modulus $E_{ribbon} = 1.54$ GPa and Poisson's ratio of 0.44. The elastomer (Ecoflex 00-50) is modeled as a hyperelastic isotropic Yeoh model. The energy density is given by

$$U = \sum_{i=1}^{N} C_{i0}(\bar{I}_1 - 3)^i + \sum_{i=1}^{N} \frac{1}{D_i}(J - 1)^{2i}$$

where $\bar{I}_1 = tr[\text{dev}(\mathbf{FF})^T]$, $J = \det(\mathbf{F})$, and $\mathbf{F}$ is the deformation gradient, and C_{i0} and D_i are the material parameters. In our model, $N = 3$, $C_{10} = 0.019$, $C_{20} = 0.0009$, $C_{30} = -4.75 \times 10^{-6}$, and $D_1 = D_2 = D_3 = 0$ (55, 56). Equal displacements ($d = 11.4$ mm, half of the distance between two wing tips) are applied in the opposite direction along the width of the pneumatic actuator to simulate the bonding process of the tips, which generated the buckled prestressed shapes without other constraints applied. The snap-through behavior is simulated using the dynamic implicit analysis with an applied pressure of 55 kPa. A damping coefficient (0.04) is added to reduce the vibration after reach to the other equilibrium state. Dynamic implicit analysis is performed for depressurization process after snapping. The minimum time step size is set to 10^{-12} to ensure the accuracy and well capture of the snap-through induced flapping. The FEA simulation procedures of the multistable flapping actuator are the same as the bistable flapping actuator, except the different initial geometric shape. The pressurization and depressurization of the four pneumatic channels were performed in sequence as shown in movie S2.

SUPPLEMENTRY MATERIALS
Supplementary material for this article is available at https://science.org/doi/10.1126/sciadv.add3788

REFERENCES AND NOTES

1. W. Shyy, H. Aono, C.-k. Kang, H. Liu, *An Introduction to Flapping Wing Aerodynamics* (Cambridge Univ. Press, 2013), vol. 37.
2. S. Ramananarivo, R. Godoy-Diana, B. Thiria, Rather than resonance, flapping wing flyers may play on aerodynamics to improve performance. *Proc. Natl. Acad. Sci. U.S.A.* **108**, 5964–5969 (2011).
3. G. K. Taylor, R. L. Nudds, A. L. R. Thomas, Flying and swimming animals cruise at a Strouhal number tuned for high power efficiency. *Nature* **425**, 707–711 (2003).
4. D. Floryan, T. V. Buren, A. J. Smits, Efficient cruising for swimming and flying animals is dictated by fluid drag. *Proc. Natl. Acad. Sci. U.S.A.* **115**, 8116–8118 (2018).
5. Y. Tang, Y. Chi, J. Sun, T.-H. Huang, O. H. Maghsoudi, A. Spence, J. Zhao, H. Su, J. Yin, Leveraging elastic instabilities for amplified performance: Spine-inspired high-speed and high-force soft robots. *Sci. Adv.* **6**, eaaz6912 (2020).
6. Y. Zhao, C. Xuan, X. Qian, Y. Alsaid, M. Hua, L. Jin, X. He, Soft phototactic swimmer based on self-sustained hydrogel oscillator. *Sci. Robot.* **4**, eaax7112 (2019).
7. T. Li, G. Li, Y. Liang, T. Cheng, J. Dai, X. Yang, B. Liu, Z. Zeng, Z. Huang, Y. Luo, Fast-moving soft electronic fish. *Sci. Adv.* **3**, e1602045 (2017).
8. G. Li, X. Chen, F. Zhou, Y. Liang, Y. Xiao, X. Cao, Z. Zhang, M. Zhang, B. Wu, S. Yin, Self-powered soft robot in the Mariana Trench. *Nature* **591**, 66–71 (2021).
9. C. Wardle, Limit of fish swimming speed. *Nature* **255**, 725–727 (1975).
10. Z. Li, N. V. Myung, Y. Yin, Light-powered soft steam engines for self-adaptive oscillation and biomimetic swimming. *Sci. Robot.* **6**, eabi4523 (2021).
11. T. Bujard, F. Giorgio-Serchi, G. D. Weymouth, A resonant squid-inspired robot unlocks biological propulsive efficiency. *Sci. Robot.* **6**, eabd2971 (2021).
12. C. S. X. Ng, M. W. M. Tan, C. Xu, Z. Yang, P. S. Lee, G. Z. Lum, Locomotion of miniature soft robots. *Adv. Mater.* **33**, e2003558 (2021).
13. Y. Forterre, J. M. Skotheim, J. Dumais, L. Mahadevan, How the venus flytrap snaps. *Nature* **433**, 421–425 (2005).
14. J. T. Overvelde, T. Kloek, J. J. D'haen, K. Bertoldi, Amplifying the response of soft actuators by harnessing snap-through instabilities. *Proc. Natl. Acad. Sci. U.S.A.* **112**, 10863–10868 (2015).
15. Y. Chi, Y. Li, Y. Zhao, Y. Hong, Y. Tang, J. Yin, Bistable and multistable actuators for soft robots: Structures, materials, and functionalities. *Adv. Mater.* **34**, 2110384 (2022).
16. S. Wu, G. L. Baker, J. Yin, Y. Zhu, Fast thermal actuators for soft robotics. *Soft Robot.* 10.1089/soro.2021.0080 (2021).
17. D. Drotman, S. Jadhav, D. Sharp, C. Chan, M. T. Tolley, Electronics-free pneumatic circuits for controlling soft-legged robots. *Sci. Robot.* **6**, eaay2627 (2021).
18. P. Rothemund, A. Ainla, L. Belding, D. J. Preston, S. Kurihara, Z. Suo, G. M. Whitesides, A soft, bistable valve for autonomous control of soft actuators. *Sci. Robot.* **3**, eaar7986 (2018).
19. T. Chen, O. R. Bilal, K. Shea, C. Daraio, Harnessing bistability for directional propulsion of soft, untethered robots. *Proc. Natl. Acad. Sci. U.S.A.* **115**, 5698–5702 (2018).
20. B. Gorissen, D. Melancon, N. Vasios, M. Torbati, K. Bertoldi, Inflatable soft jumper inspired by shell snapping. *Sci. Robot.* **5**, eabb1967 (2020).
21. E. Zereik, M. Bibuli, N. Mišković, P. Ridao, A. Pascoal, Challenges and future trends in marine robotics. *Annu. Rev. Control* **46**, 350–368 (2018).
22. C. Christianson, N. N. Goldberg, D. D. Deheyn, S. Cai, M. T. Tolley, Translucent soft robots driven by frameless fluid electrode dielectric elastomer actuators. *Sci. Robot.* **3**, eaat1893 (2018).
23. D. Q. Nguyen, V. A. Ho, Anguilliform swimming performance of an eel-inspired soft robot. *Soft Robot.* **9**, 425–439 (2022).
24. H. Niu, R. Feng, Y. Xie, B. Jiang, Y. Sheng, Y. Yu, H. Baoyin, X. Zeng, Magworm: A biomimetic magnet embedded worm-like soft robot. *Soft Robot.* **8**, 507–518 (2021).
25. A. D. Marchese, C. D. Onal, D. Rus, Autonomous soft robotic fish capable of escape maneuvers using fluidic elastomer actuators. *Soft Robot.* **1**, 75–87 (2014).
26. M. D. Bartlett, N. Kazem, M. J. Powell-Palm, X. Huang, W. Sun, J. A. Malen, C. Majidi, High thermal conductivity in soft elastomers with elongated liquid metal inclusions. *Proc. Natl. Acad. Sci. U.S.A.* **114**, 2143–2148 (2017).
27. T. L. Hedrick, B. W. Tobalske, I. G. Ros, D. R. Warrick, A. A. Biewener, Morphological and kinematic basis of the hummingbird flight stroke: Scaling of flight muscle transmission ratio. *Proc. R. Soc. B Biol. Sci.* **279**, 1986–1992 (2012).
28. S. E. Farisenkov, D. Kolomenskiy, P. N. Petrov, T. Engels, N. A. Lapina, F.-O. Lehmann, R. Onishi, H. Liu, A. A. Polilov, Novel flight style and light wings boost flight performance of tiny beetles. *Nature* **602**, 1–5 (2022).
29. C. Zhang, C. Rossi, A review of compliant transmission mechanisms for bio-inspired flapping-wing micro air vehicles. *Bioinspir. Biomim.* **12**, 025005 (2017).
30. Y. Chen, H. Zhao, J. Mao, P. Chirarattananon, E. F. Helbling, N.-S. P. Hyun, D. R. Clarke, R. J. Wood, Controlled flight of a microrobot powered by soft artificial muscles. *Nature* **575**, 324–329 (2019).
31. G. M. Whitesides, Soft robotics. *Angew. Chem. Int. Ed.* **57**, 4258–4273 (2018).
32. R. Tǎiar, P. Sagnes, C. Henry, A. B. Dufour, A. H. Rouard, Hydrodynamics optimization in butterfly swimming: Position, drag coefficient and performance. *J. Biomech.* **32**, 803–810 (1999).
33. P. Furmanek, J. M. Redondo Apraiz, À. García Carrillo, J. D. Tellez Alvarez, R. Arellano, Experiments and simulations of maximal sculling propulsion: vorticity impulse in human biomechanics, in *Proceedings Topical Problems of Fluid Mechanics 2016* (2016), pp. 41–50.
34. S. Taormina, *Swim Speed Strokes for Swimmers and Triathletes: Master Freestyle, Butterfly, Breaststroke and Backstroke for Your Fastest Swimming* (VeloPress, 2014).
35. S. Jung, Swimming, flying, and diving behaviors from a unified 2D potential model. *Sci. Rep.* **11**, 15984 (2021).
36. G. Li, I. Ashraf, B. François, D. Kolomenskiy, F. Lechenault, R. Godoy-Diana, B. Thiria, Burst-and-coast swimmers optimize gait by adapting unique intrinsic cycle. *Commun. Biol.* **4**, 1–7 (2021).
37. B. D. Clark, W. Bemis, Kinematics of swimming of penguins at the Detroit Zoo. *J. Zool.* **188**, 411–428 (1979).
38. B. R. Mate, B. A. Lagerquist, J. Calambokidis, Movements of north pacific blue whales during the feeding season off Southern California and their southern fall migration. *Mar. Mamm.* **15**, 1246–1257 (1999).
39. F. E. Fish, A. Kolpas, A. Crossett, M. A. Dudas, K. W. Moored, H. Bart-Smith, Kinematics of swimming of the manta ray: Three-dimensional analysis of open-water maneuverability. *J. Exp. Biol.* **221**, jeb166041 (2018).
40. M. Riedman, *The Pinnipeds: Seals, Sea Lions, and Walruses* (University of California Press, 1990), vol. 12.
41. G. Díez, M. Soto, J. Blanco, Biological characterization of the skin of shortfin mako shark *Isurus oxyrinchus* and preliminary study of the hydrodynamic behaviour through computational fluid dynamics. *J. Fish Biol.* **87**, 123–137 (2015).
42. J. Davenport, Observations on the locomotion of post-larval and juvenile flying fish. *J. Mar. Biolog. Assoc. U.K.* **70**, 311–320 (1990).
43. T. Iwai, M. Hisada, *Fishes—Illustrated Book of Gakken* (1998).
44. W. T. White, J. Giles, I. C. Potter, Data on the bycatch fishery and reproductive biology of mobulid rays (*Myliobatiformes*) in Indonesia. *Fish. Res.* **82**, 65–73 (2006).
45. J. Iriarte-Díaz, Differential scaling of locomotor performance in small and large terrestrial mammals. *J. Exp. Biol.* **205**, 2897–2908 (2002).
46. D. Hwang, E. J. Barron, A. B. M. T. Haque, M. D. Bartlett, Shape morphing mechanical metamaterials through reversible plasticity. *Sci. Robot.* **7**, eabg2171 (2022).
47. D. Walker, B. T. Käsdorf, H.-H. Jeong, O. Lieleg, P. Fischer, Enzymatically active biomimetic micropropellers for the penetration of mucin gels. *Sci. Adv.* **1**, e1500501 (2015).
48. K. N. Lucas, N. Johnson, W. T. Beaulieu, E. Cathcart, G. Tirrell, S. P. Colin, B. J. Gemmell, J. O. Dabiri, J. H. Costello, Bending rules for animal propulsion. *Nat. Commun.* **5**, 1–7 (2014).
49. R. Chen, Z. Yuan, J. Guo, L. Bai, X. Zhu, F. Liu, H. Pu, L. Xin, Y. Peng, J. Luo, L. Wen, Y. Sun, Legless soft robots capable of rapid, continuous, and steered jumping. *Nat. Commun.* **12**, 7028 (2021).
50. Y. Wu, J. K. Yim, J. Liang, Z. Shao, M. Qi, J. Zhong, Z. Luo, X. Yan, M. Zhang, X. Wang, Insect-scale fast moving and ultrarobust soft robot. *Sci. Robot.* **4**, eaax1594 (2019).
51. T. Helps, C. Romero, M. Taghavi, A. T. Conn, J. Rossiter, Liquid-amplified zipping actuators for micro-air vehicles with transmission-free flapping. *Sci. Robot.* **7**, eabi8189 (2022).
52. W. Hu, G. Z. Lum, M. Mastrangeli, M. Sitti, Small-scale soft-bodied robot with multimodal locomotion. *Nature* **554**, 81–85 (2018).
53. Y. Kim, H. Yuk, R. Zhao, S. A. Chester, X. Zhao, Printing ferromagnetic domains for untethered fast-transforming soft materials. *Nature* **558**, 274–279 (2018).
54. A. Kotikian, C. McMahan, E. C. Davidson, J. M. Muhammad, R. D. Weeks, C. Daraio, J. A. Lewis, Untethered soft robotic matter with passive control of shape morphing and propulsion. *Sci. Robot.* **4**, eaax7044 (2019).
55. Y. Tang, Q. Zhang, G. Lin, J. Yin, Switchable adhesion actuator for amphibious climbing soft robot. *Soft Robot.* **5**, 592–600 (2018).
56. Y. Chi, Y. Tang, H. Liu, J. Yin, Leveraging monostable and bistable pre-curved bilayer actuators for high-performance multitask soft robots. *Adv. Mater. Technol.* **5**, 2000370 (2020).